Title

Studies of a prototype linear stationary x-ray source for tomosynthesis imaging

Journal

Physics in Medicine and Biology, 59(10)

ISSN

0031-9155

Authors

Schwoebel, PR
Boone, John M
Shao, Joe

Publication Date

2014-05-21

DOI

10.1088/0031-9155/59/10/2393

Peer reviewed

Published in final edited form as:
Phys Med Biol. 2014 May 21; 59(10): 2393–2413. doi:10.1088/0031-9155/59/10/2393.

Studies of a prototype linear stationary X-ray source for tomosynthesis imaging

P R Schwoebel[1], **John M. Boone**[2], and **Joe Shao**[2]

P R Schwoebel: paul.schwoebel@sri.com

[1]SRI International, 333 Ravenswood Avenue, Menlo Park, CA 94025, USA

[2]Department of Radiology, 4860 Y Street, Ambulatory Care Centre, University of California-Davis, Sacramento, CA 95817, USA

Abstract

A prototype linear X-ray source to implement stationary source – stationary detector tomosynthesis imaging has been studied. Potential applications include human breast and small animal imaging. The source is comprised of ten X-ray source elements each consisting of a field emission cathode, electrostatic lens, and target. The electrostatic lens and target are common to all elements. The source elements form X-ray focal spots with minimum diameters of 0.3 to 0.4 mm at electron beam currents of up to 40 mA with a beam voltage of 40 kV. The X-ray flux versus time was quantified from each source. X-ray bremsstrahlung spectra from tungsten targets were produced using electron beam energies from 35 to 50 keV. The half-value layer was measured to be 0.8 mm, 0.9 mm, and 1.0 mm, respectively, for the 35 kV, 40 kV, and 45 kV tube potentials using the tungsten target. The suppression of voltage breakdown events, particularly during source operation, and the use of a modified form of the standard cold-cathode geometry, enhanced source reliability. The prototype linear source was used to collect tomographic data sets of a mouse phantom using digital tomosynthesis reconstruction methods and demonstrated a slice-sensitivity profile with a full-width-half-maximum of 1.3 mm. Lastly, preliminary studies of tomographic imaging of flow through the mouse phantom were performed.

Keywords

Stationary X-ray source; Digital tomosynthesis; Tomographic medical imaging; Vascular dynamics

1. Introduction

Tomosynthesis (TS) is most widely used for breast imaging (Niklason 1997, Alakhras 2013) but has been developed commercially for abdominal imaging and is being investigated for applications such as the detection of lung metastasis (Jung 2012). In breast imaging, TS is performed using 15 to 30 projection images over angles of 15° to 30° (Sechopoulos, 2013). Using a stationary detector geometric approach to TS (Niklason *et al*., 1997), a stationary X-ray source array would eliminate all motion. This not only makes the mechanical construction of the TS system much more straightforward, but the limitations of mechanically moved imaging components, such as speed and flexibility in angular coverage,

are eliminated (Tucker *et al*., 2013). Because mechanical vibration and source motion are removed, image quality is also potentially improved and system complexity, size, and cost may be decreased. Potential advantages of a stationary X-ray source were realized early and applied to both cardiac imaging and fluoroscopy (Fahrig *et al*., 2005, Bushberg 2012) using scanned beam systems which, although highly capable, are either large and expensive, or not easily scalable.

More recently the potential of both multi-source and stationary sources in the form of addressable arrays of individual x-ray sources is being evaluated by several research groups for diagnostic imaging (Uribe *et al.* 2010, Qian *et al*. 2012, Hsieh *et al*. 2013, Xu *et al.* 2011, Shan *et al.* 2013), image guided therapy (Maltz *et al.* 2009) and small animal radiation therapy applications (Schreiber *et al*. 2012). Multi-source and stationary X-ray source approaches can be closely related. Multi-sources can be used with motion of the multi-source to increase imaging speed, reduce the amount of angular translation required and tailor X-ray beam qualities of the individual source forming the multi-source. One of the more advanced multi-source systems employs 32 X-ray sources based on electron tube dispenser (i.e. thermionic) cathode technology and has been demonstrated in a conventional inverse geometry CT (Uribe *et al.* 2010). In principle, stationary sources based on thermionic cathodes could be employed in a grid-controlled configuration (Toshiba 2014) to address and pulse individual sources at kilohertz type frequencies.

Presently, stationary x-ray sources under development are mostly based on cold field emission cathodes. The use of cold cathodes avoids complications due to power handling with arrays of thermionic cathodes. The cold cathodes that have been most generally studied in a wide variety of applications are the Spindt-type, based on metal field emission tips, and those using carbon nanotube (CNT) emitter tips (Xu and Huq 2005, Saito 2010).

A significant focus of the recent work on CNT emitter tip cathodes has been in the area of flat-panel displays and x-ray sources (Saito 2010) whereas Spindt tips are most actively being applied to high performance microwave tubes (Whaley 2009). The interest in CNT-based stationary x-ray sources has stemmed from the fact that they can provide currents and current densities similar to that achieved by the conventional tungsten filament cathodes in x-ray tubes, ~1 A/cm^2 (Brodie and Muray 1992) at roughly ≤1 A while appearing to be moderately robust in the x-ray tube environment (Saito 2010). Part of the robustness of these cathodes is due to their use of a non-integral gate (grid) electrode which requires extraction voltages of the order of 1 kV (Qian *et al.* 2012). The lifetime and stability of CNT cathodes under various conditions remains under investigation (see for example Saito 2010 and Smith *et al.* 2013).

The interest in applying Spindt cathodes to high performance microwave tubes is in a large part due to the benefits of employing an integrated gate electrode (Brodie and Spindt 1992) which are two fold: 1) High current densities are achievable with high total currents, for example 0.3 A at 40 A/cm^2 from a 1-mm diameter cathode (Schwoebel 2005) and 2) High transconductance and direct beam modulation at frequencies in excess of 1 GHz with modest voltages (< 100 V) (Jensen 1999, Whaley *et al.* 2002). Many of these characteristics could also be beneficial in the application of Spindt-type cathodes to X-ray tubes. Low

control voltages simplify and decrease the cost of cathode blanking circuitry. The high total currents demonstrated to date provide more total current than is needed for most medical imaging applications, except thus far, the highest current CT tubes (Note that in existing well-designed x-ray tubes the beam currents are limited by anode power handling limitations (Bushberg 2012)). The high current densities imply that the currents required can be extracted from a smaller area relative to cathodes with lower current densities. Thus in possible future applications, in which cathode-to-cathode distances are small, say in a high source density multi-source or stationary source CT system, these cathodes could still supply the current required. Lastly, the semiconductor microfabrication techniques used to fabricate the cathodes allow for inexpensive manufacturing and straightforward tailoring of their geometrical shape to the application, i.e. a rectangular arrays to more easily exploit the line focus principle for anode power handling considerations. On the other hand, the integral gate electrode which helps to bestow so may of these attractive properties also makes the cathode more subject to damage by electrical breakdown events (Schwoebel and Brodie 1995). Thus evaluation of reliability is an important component of the present investigations directed at the use of these cathodes in medical x-ray imaging applications.

We have already investigated the performance of an individual x-ray element that would be arrayed to form a stationary source (Schwoebel 2006) based on Spindt cathodes. In the present studies the stationary source is comprised of an array of such individual X-ray source elements. TS data are accumulated by addressing each source element comprising the stationary source in a serial manner and storing the image data from the flat-panel detector in computer memory before operating the subsequent source. An immediate goal of this work is to develop a real-time TS system for dynamic vascular imaging in the small animal by integrating the stationary X-ray source technology with a flat-panel detector (see Figure 1). The potential is to increase the temporal resolution over that of CT scanners by reduced scan time as limited by both x-ray source flux and detector frame rate, with possibly decreased cost.

In this paper we discuss the basic design of the stationary source and measurements of the electron beam current, X-ray spot size, half-value layer, X-ray energy spectra and reliability. The studies conclude by using the stationary source-stationary detector system to accumulate tomographic data sets of a mouse flow phantom, measure the slice sensitivity profile, and reconstruct the data to generate a series of tomographic images. Small animal imaging with high temporal resolution is a challenging goal (Badea *et al*., 2010), due to the very rapid heart-rates of small animals. The use of stationary X-ray source arrays may prove useful towards this goal. Lastly, preliminary studies of imaging of flow through the mouse phantom were performed.

2. Methods

X-ray source studies were conducted using a stainless steel and glass actively pumped vacuum chamber to house the stationary X-ray source, resulting in a custom X-ray tube operating in the low 10^{-10} Torr range following a 12 h bake-out at 200 °C.

The stationary source is made up of 10 individual X-ray source elements. Each source element consists of a field electron source, electron lens, and a tungsten anode target. The electron source for each X-ray source element was a 50,000-tip Spindt-type field emission cathode made at SRI International and mounted on TO-5 headers, see Figure 2. The tips were distributed over a circular area with a 1 mm diameter, i.e. an area of 0.8 mm^2. The metal gate film was insulated form the tips by thermally grown SiO_2 (nominal d.c. dielectric constant = 4 and bulk dielectric strength ~ 5×10^6 V/cm see Maissel and Glang 1970) The metal gate film electrode was grounded and the tip electrode (silicon base) was operated between roughly −100 V and −250 V to extract the desired electron current. This choice of polarity is fundamentally arbitrary. The cathodes used in the majority of these experiments had been previously qualified to emission current levels of at least 10 mA, i.e. 1.25 A/cm^2, prior to installation in the stationary source. Prequalification, i.e. initial cathode turn-on and subsequent operation at 10 mA, typically involves gradually increasing the current from μA-level to mA-level currents over the period of two to three days. Following this initial prequalification the cathodes were installed in the stationary source, the source was baked and the cathodes were further conditioned over the period of ~1 day, which also outgassed the target anode, before high-current operation (10 mA to 40 mA) experiments were initiated.

As discussed in sections 3.6 and 4.6 below, due to cathode failures in the high-power, high-voltage environment of the stationary X-ray source, completing the entire set of source characterization studies presented here without changing out some failed source elements during the course of the experiments was not possible. Operating at reduced electron beam current and/or anode voltage, i.e. X-ray tube power, levels significantly enhanced reliability, as discussed in Sections 3.6 and 4.6 below. Thus some experiments were conducted at lower power levels in order to insure that multiple measurements could be made under identical conditions for comparison with one another. The full set of experiments reported here was not completed without at least one source replacement when running a full set of 10 sources. However, we were able to complete all of the experiments reported here using a cathode set in which the first source element was electrically shorted during high current operation while the remaining nine persisted with reliable source operation for the roughly 200 hours required (including conditioning time).

A schematic diagram and photograph of the stationary X-ray source is shown in Figure 3. The distance between the source elements, i.e., the X-ray focal spots on the anode, was 1 cm. An electrostatic lens assembly was used to form electron beam focal spots on the target anode. This electrostatic lens was comprised of an acceleration electrode following the cathode at a distance of 0.5 cm, a focus electrode 0.5 cm distant from the acceleration electrode and lastly the target anode, 1.5 cm distant from the focus electrode. The anode target was a tungsten rod 15-cm in length and 1.27-cm in diameter, ground flat on one side. The anode was both hydrogen and vacuum fired at 1000 °C for 1 hr prior to installation in the tube to reduce outgassing. The target anode was operated at voltages between 35 kV and 50 kV with respect to ground. A potential of 50 kV is the approximate upper voltage that can be used for reliable operation of the X-ray source in its present design. Above 50 kV voltage breakdown occurs within the vacuum envelope. Image intensified visual observations of the pre-breakdown phenomena indicate that electron emission from the

focus electrode (see Figure 3) precipitates the ultimate breakdown of the anode voltage. The target was tilted at an angle of 20° with respect to the electron beam axis and the detector was placed at 40° with respect to the electron beam axis. Note that for these prototyping studies, no beam collimation was employed as the system was operated in an unoccupied room.

The X-ray source elements were operated by an in-house, custom-built source controller. The source controller defined the electric potential between the tip and gate electrodes (i.e. emission current) for each X-ray source element. It could also be used to vary electron (X-ray) pulse widths from each source element from 1 ms to 1 s and all ten source elements could be fired in sequence at rates varying from 1 element per second to 10^3 element/s. In principle the linear source can thus provide one complete tomographic data set (i.e. one image from each of the 10 source elements) at rates ranging from 0.1 Hz to 100 Hz.

The detector was a Varian PAXSCAN 1313 which uses an indirect thin-film transistor design and a CsI scintillator. The 1313 panel incorporates 127 μm pixels over a 13 cm × 13 cm field of view, appropriate for mouse imaging at near-unity magnification. The array of 1024 × 1024 pixels can be read out at up to 30 frames per second. The electronics associated with the flat-panel detector provides a 5 V transistor-to-transistor logic (TTL) pulse for each frame, and this TTL pulse was integrated with the source controller to synchronize the firing of each X-ray source element. Niklason (personal communication) has demonstrated that an anti-scatter grid is not necessary on digital imaging systems when the object (breasts in his analysis) is thinner than about 5 cm, and therefore an anti-scatter grid was not used in these experiments using phantoms approximating the dimensions of small animals. Anticipating future vascular dynamics studies in small animals (see below), an X-ray focal spot-to-detector distance of between 10 and 25 cm was used.

Fundamental operating parameters of the X-ray source investigated here were the electron emission current from the cold cathode versus voltage applied to the cathode and versus time, the X-ray focal spot size, the X-ray energy distribution and half-value layer, and lastly the slice sensitivity profile. Electron beam currents on the target anode were measured using an integrated signal from a Stangness Model 0.5 – 1.0W current transformer. X-ray pulse shape versus time measurements were taken using an Amperex XP2262B photomultiplier tube and plastic scintillator with the output viewed directly on a Tektronix TDS540D oscilloscope. X-ray pulse duration and repetition rate studies were conducted at 10 Hz and 30 Hz, the standard operational rates of the detector. Pulse widths used were 10 ms and 50 ms, respectively, at the 10 Hz and 30 Hz rates for the detector. X-ray focal spot sizes were measured at 6× magnification with a Nuclear Associates 10 μm diameter pinhole. The spots were viewed at an angle of 20° to the normal of the anode surface. As the electron beam was incident at an angle of 20° to the normal of the anode surface, the angle between the electron beam and the spot viewing (or centre of the object) location was 40°. The pinhole was placed in a 2.5-cm thick aluminium holder. X-ray focal spot images were recorded using Kodak Min-R2 cassettes. X-ray spectra were measured using an Amptek XR-100 detector calibrated with ^{55}Fe and ^{241}Am X-ray standards. X-ray half-value layer (HVL) measurements were made using one source element and a Radcal 10X9-6M ionization chamber with a set of aluminium filters. The chamber is calibrated by the manufacturer

every two years with procedures traceable to NIST standards. Measurements were conducted with X-ray tube potentials of 35 kV, 40 kV, and 45 kV.

Data sets for TS reconstruction were acquired of a mouse phantom resting on the detector, with near-unity magnification. The linear X-ray source was centred between source elements 5 and 6 on the phantom. The distance between elements 5 and 6 and the phantom was 22 cm providing an angular coverage of ±12°, i.e. a tomographic angle of 24°. As this is a proof-of-principle study the development of an optimal phantom for measuring geometric calibration, and the associated software for evaluating the phantom information, was not done. Without a full geometric calibration of the imaging system (*e.g*. Yang, *et al*., 2006) filtered backprojection (Bushberg, 2012) or matrix inversion (Godfrey *et al*., 2013) techniques were not possible. Hence, TS reconstruction was performed using the shift and add method (Niklason *et al.* 1997), which is more robust when geometric factors are known with reduced precision. The linear source array repeated acquisition at 33 ms frame times from source 1 to source 10. While the time window for the acquisition of a complete tomosynthesis projection data set required 330 ms, these images could be updated every 33 ms by updating the data set with the most recent single source acquisition projection image. Thus, the temporal resolution of this approach is described by a 330 ms travelling window in time, updated every 33 ms (30 Hz). As mentioned above, the temporal resolution in this set-up is related to the detector frame rate, and faster detector systems would be capable of higher bandwidth imaging.

All tomographic and flow imaging was conducted at an anode target voltage of 40 kV. The mouse flow phantom was a 12-mL Kendal Monoject syringe wrapped with tubing from a TopSpins contrast and flush set (see Figure 4). The tubing had an outside diameter of 2 mm and an inside diameter of 1.2 mm. A mouse skull was included for a size reference. The iodine contrast agent used in the flow phantom was GE Healthcare Visipaque (ioduxanol) injected at a concentration of 320 mgI/mL. Flow-rates through the phantom were controlled manually. Consistency of flow within a given experiment was within roughly 10% as determined by viewing changes in flow rate based on source element firing rate during washout. Tomographic data sets were accumulated at a rate of 30 frames/second, i.e. one complete tomographic data set in 1/3 second).

3. Results

3.1. Electron emission current

An example of a cathode electron current-voltage emission characteristic for a single source element (*I-V*; emission current, *I*, versus gate voltage, *V*, applied to the cathode) is shown in Figure 5 and reflects the expected exponential character of the *I-V* characteristic (Brodie and Schwoebel 1994). The current measured on the gate electrode with 150 mA on the target was less than 10 μA. Such small fractional gate currents are typical if the cathodes are operating properly. The maximum emitted current shown corresponds to a current density of 19 A/cm^2. These tests were performed at 10 kV target voltages with the beam defocused on the anode target to mitigate target damage by overheating. Current pulse widths of 1 ms at 1 Hz with several pulses at each cathode tip voltage were used for the data in Figure 5. There is some variation in the *I-V* characteristics from array to array, i.e. some may achieve 100

mA of emission current at −100 V and others may require upwards of −200 V to achieve the same emission current. To compensate for this variation, the voltage on each array element is adjusted with the source controller such that the emission current from each source element is the same. The focal properties of the electrostatic lens in the X-ray source were not sensitive to variations in cathode operating voltage range (−150 V ± 100V) for a given current.

3.2. X-ray pulse shape measurement

The shape of the X-ray pulses from each source element was viewed at pulse lengths and repetition rates used for the collection of TS data. Figure 6 shows typical examples of the appearance during the acquisition of a tomographic data set taken at 10 mA (electron current) with an accelerating potential of 40 kV at a rate of 10 Hz with an X-ray pulse width of 50 ms. At this pulse width some anode melting under the beam spot was evident following removal from the vacuum system. Acquisition protocols at 30 Hz used an X-ray pulse width of 10 ms. As noted in the Methods Section, 10 Hz and 30 Hz are the standard readout rates of the X-ray detector used for TS imaging. These results are consistent and constant within ~±5% over the time periods of several hours studied to date for pulse widths in the range of ~ 1 ms to 0.1 s with no obvious connection to cathode lifetime, see Section 3.6. The stability with time for pulse widths greater than 0.1 s, or at various pulse widths as a function of frequency will be studied in the future. At higher power levels, i.e. 40 mA at 40 kV with pulse widths reduced to 1ms to prevent anode overheating, similar curves are obtained, but reliability at this power level was erratic – with at times no cathode element failures for several hours before termination of the experiment, or sudden failure of a cathode element after just a few 10s of minutes at high power levels. Additional studies of variations over longer time periods at high power levels will be conducted in the future.

3.3. X-ray focal spots

X-ray focal spot sizes were measured at electron beam potentials of 40 kV and current levels of up to 40 mA using current pulse widths of 1 ms at 1% duty cycle to prevent anode damage. The 40 kV/40 mA combination was chosen to demonstrate the focal spot size as this combination provides the maximum flux useable, as at the corresponding X-ray flux the exposure rate of the TS system becomes limited by the download time of existing detector technology, as discussed in detail in Section 4.1 below.

The focal spot size was insensitive to the anode voltage for voltages between ~10 kV and 50 kV. Figure 7 shows a focal spot and the associated plot of optical density versus position in the spot. The horizontal and vertical reticules on the edge of the photograph of the X-ray spot define the horizontal and vertical lines through the spot that correspond to the plots shown in Figure 7b of density versus position. The horizontal axis is along the length of the anode rod. 90% of the electrons are contained within a spot having a width of 0.26 mm and height of 0.38 mm. Due to the system symmetry, the X-ray focal spots from each source element did not vary by much with all 10 spots from one linear source showing an average of 0.26 mm ± 0.04 mm in width and 0.38 mm ± 0.06 mm in height.

3.4. X-ray spectra

Tungsten is a standard target used in both breast digital TS and small animal imaging systems. In these studies X-ray spectra from the tungsten target anode were measured at anode voltages of 35, 40, 45, and 50 kV, see Figure 8. Essentially standard bremsstrahlung spectra with evidence of the tungsten *L*-lines at 9 to ~11 keV are observed. Some unresolved *K*-lines from source structural components appear centered around 5 keV.

3.5. Half-value layer measurement

HVL measurements were made as a function of tube potential from 35 kV through 45 kV. Figure 9 is a plot of X-ray tube potential versus HVL. The effective beam energy corresponding to the HVLs (Bushberg *et al.* 2012) is also shown and corresponds to 0.8 mm, 0.9 mm, and 1.0 mm being equivalent to an effective beam energy of, respectively, 20 keV, 21 keV, and 22 keV.

3.6. Source time to failure

Failure was taken as a significant change in the operational characteristics of the cathode and was most often due to a low resistance electrical short between the gate and tip electrodes. Failure modes varyied from graceful, through gradual changes in the current-voltage characteristics of the cathode in the source element, to catastrophic with sudden complete destruction of the cathode structure. Both historically and during the course of these experiments, the cathode lifetime tended to decrease as the emitted current is increased beyond levels of the order of 10 mA (corresponding to an emission current density of roughly 1 A/cm^2), particularly when high electrostatic fields (or high voltages) were present on electrodes adjacent to the cathode, as the combination tends to precipitate voltage breakdown. This trend was observed even when highly defocused electron beams impinge on the collector (target) electrode used so that collector temperatures remain near room temperature (Schwoebel and Brodie 1995). Visual damage was often evident and frequently consisted of melting and vaporization of gate film surrounding the tips and even removal of all evidence of tips and gate film, revealing the underlying silicon substrate on which the cathode was constructed.

Of the approximately 200 cathodes tested in the stationary source, roughly 100 suffered from some mode of failure with ~50 suffering catastrophic failure. Over the course of the nearly 100 such failures, times to failure ranged from less than 10 minutes to greater than 50 hours of source operational time, so statistical scatter is too large to determine a useful mean time to failure. With some cathode elements, 100 mA was easily and reliably achieved over many hours of operation even at target voltages of 40 kV (The beam was defocused and duty cycle decreased to typically ~ 1% using pulse durations of 1 ms to preclude target melting under these high current conditions). With others, currents exceeding on the order of 10 mA could lead to cathode damage. We have not yet correlated any possible dependence of the failure rate (i.e. lifetime) or emitted current stability on current pulse width with current pulse repetition frequency as a parameter.

Besides high current operation possibly leading to voltage breakdown damage was infrequently caused by exposure of the source elements to atmosphere (say for replacement

of a source element) or other as-yet-unidentified processes. In some cases failure of the cathode in one source element during operation would induce failure in one or more other (not necessarily physically adjacent) cathode source elements. Such damage appeared to take basically two forms. In the first either little to no visible damage was evident, yet the tip and gate electrodes were electrically shorted. Here deposition of vaporized electrode material onto cathode insulating surfaces as the result of the breakdown evident was suspected. In the second, cathode damage was clearly visually evident, often appearing much like the case in which the cathode was damaged during operation. In this case it is inferred that a voltage pulse as the result of breakdown elsewhere in the system was coupled into the cathode resulting in its over-voltage (in either polarity).

Cathodes employing a Si_2N_3 dielectric shield (nominal d.c. dielectric constant = 7, dielectric strength ~ 10^7 V/cm see Maissel and Glang 1970) interposed between the tip and gate electrodes, see Figure 10, inhibited, relative to the standard design, the development of electrical shorts between the tip and gate electrodes following minor damage to the cathode, for example after destruction of a few tips within an array. Even some of the more destructive damage wherein significant fractions of the cathode are destroyed by an electrical discharge removing some tips did not result in sufficient gate-to-tip electrode electrical leakage to prevent continued operation of the cathode, i.e. the failure as more graceful than with the standard Spindt cathode design. Of the ~200 cathodes tested, 139 employed the dielectric shield. Of these roughly one-third had some sort of failure and of these roughly one-half failed gracefully with the development of tip-to-gate electrode leakage as discussed above. From these numbers one can see that this cathode design improves reliability over that of the standard design.

3.7. Slice Sensitivity Profile

The slice sensitivity profile at a beam current of 10 mA and an X-ray tube potential of 40 kV was measured to have a full-width-half-maximum (FWHM) of 1.27 mm. While the slice spacing is finer than this, the limited angle nature of TS results in thicker tomographic slices than for complete-angle tomographic imaging where the tomographic angle of acquisition exceeds 180° plus the fan angle (Nosratieh *et al*, 2012). Although this is a limitation when compared to true tomography, the pseudo-tomographic effect that is provided by TS methods has been found to be a useful adjunct over pure projection imaging.

3.8. Flow phantom imaging and tomosynthesis

Reconstructed data sets of the mouse flow phantom were accumulated with the phantom resting on the detector (essentially unity magnification) and reconstructed using a simple shift-and-add method. Figure 11 shows a selection of tomographic images for the case in which the phantom is loaded with contrast agent. One can see that different tomographic planes are in focus in each image. This is made more evident by examination of the enlarged views of the skull in the sagittal projection associated with each image. In Figure 11a the molars on the right side of the jaw are in focus, In Figure 11c the molars on the left side of the jaw are in focus. In Figure 11b the focal plane lies between those shown in Figures 11a and 11c. The reconstructed data set can be viewed in its entirety in the supplementary data file of the online paper.

Tomographic data sets were also collected at a rate of one data set per 330 ms, while contrast agent flowed through the phantom. Figure 12 shows a series of images of one projection from each data set. Here the phantom was filled with contrast agent, tomographic data accumulation was initiated and water was used to replace the contrast agent (washout). In Figure 12 one can see that the contrast agent is gradually flushed from the phantom (from left to right) at a flow rate of 0.2 cc/s. In Figure 12a the tubing surrounding the syringe is full of contrast agent, In Figure 12b the arrow shows the water contrast agent boundary, and lastly in Figure 12c the tubing is full of water. The time interval between 12(a) and 12(b) being 1/3 s, and that between 12(b) and 12(c) being 2/3 s. A movie showing the complete set of these single projections as a function of time in 1/3 s intervals, in which near real-time flow through the phantom can be visualized, is available as supplementary material in the online version of this paper. The reconstructed data sets allow one to just discern the flow of contrast agent through the phantom, and are also available for viewing as supplementary material in the online version of this paper.

4. Discussion

4.1. Electron current

The X-ray flux is directly proportional to the electron current impinging on the anode target electrode for a given target material and source-object-detector geometry at a given electron energy. Thus these currents produce an X-ray fluence that is linearly proportional to the mA multiplied by the time (mAs). Small animal and breast digital TS systems typically require electron beam currents of up to 25 – 100 mA. It has thus been demonstrated that the microfabricated cathodes can provide current levels necessary for these tomographic imaging applications with the caveats discussed in Sections 3.6 and 4.6.

For our system prototyping studies with a small-animal imaging stationary source, an exposure of roughly 10 μGy *at the detector* for each of the 10 views is required to form the tomographic image. To estimate the maximum currents required for our system we can assume that at 40 kVp the X-ray tube output with 2 mm of aluminum filtration is ~2.5 mGy/100 mAs @ 1 m (Bushberg 2012). For mouse imaging, with the mouse resting on the detector (i.e., essentially unity magnification), a source-to-detector distance of ~10 cm can be used. Thus the source output is now (10^2 × 2.5 mGy/100 mAs) 250 mGy/100 mAs @ 10 cm. Including a mouse attenuation factor of ~10 we have an air kerma rate at the detector of 25 mGy/100 mAs. Thus for a minimum exposure time of, for example, 1 ms (i.e. accumulating one complete tomographic data set at a rate of 100 Hz) a current of ~40 mA is required. At this level, our prototype system would be limited by the detector download time, as discussed further below in Section 4.8.

4.2. X-ray pulse shape measurement

The pulse shape between different pulses showed some variability with peak currents remaining within ~ ± 2.5% between tomographic data sets (i.e. firing of all 9 source elements) for a given source element (Figure 6). These measurements were conducted without feedback between the controller and target current measurement. The controller voltage was simply set such that each source element provided a similar current (i.e. X-ray

flux) and sequential operation was initiated without further adjustments to the controller voltage. The slight changes in the X-ray flux from each source element are then due to slight changes in the emission current from each element. Changes in the emission current, under these circumstances is due to the adsorption and desorption of background gas phase species on the tip surfaces. This was a reversible process as on the average we did not observe a net change in the emission current with time. As mentioned in the Results section, longer-term operational studies will be conducted in order to determine if such a net trend may emerge.

4.3. X-ray focal spots

Elongation of the spot in the vertical direction as shown in Figure 7 is the result of the 20° angle at which the electron beam is directed relative to the normal to the surface of the anode. The fact that the detector was set an angle of 40° relative to the axis of the beam means that the spot size at the detector is as it appears on the anode with no influence due to the line focus principle. The focal spot can thus be decreased in the vertical direction of Figure 7 by increasing the angle between the beam axis and the normal to the detector. For example, the effective X-ray focal spot size would be 0.26 mm × 0.26 mm if the angle between the electron beam axis and the detector was increased to ~ 67°. On-going studies are being performed to quantify the spot size and heel effect at various relative beam-axis target and detector angles.

X-ray focal spots with a circular spot or, for greater anode target power handling capability a line focus, are possible with this source. The electrostatic lens employed here was designed for a circular focus to simplify the prototype source configuration. A line focus is most easily implemented by fabricating the source such that it provides an electron beam with a rectangular cross-section on the anode.

Ultimately the spot shape used is determined by the power density dissipation needs, which are in turn defined by the required X-ray flux, fluence, effective spot size, and number of source elements that comprise the stationary source. For functional imaging studies in small animals, an effective focal spot with roughly a 0.2 mm diameter is adequate (Badea 2008). Maximum power (minimum exposure times) is achieved using a line focus which for an effective 0.2 mm diameter spot requires a 0.2 mm × ~1 mm spot roughly equivalent in area to a circular focal spot diameter of ~0.5 mm (= $2\sqrt{(1\text{ mm} \times 0.2\text{ mm}/\pi}$]). The time to reach 0.8 times the melting point of a W target is then of the order of 1 ms (Muller 1931) at 40 kV and 40 mA roughly the exposure time required for the mouse TS system to be exposure rate limited by the download time of existing detector technology, see Section 4.1 and 4.8.

4.4. X-ray spectra

The bremsstrahlung X-ray spectra shown in Figure 8, are essentially standard spectra expected from tungsten when filtered through the glass envelope of the X-ray tube. The low energy peak between ~ 5 and 7 keV is associated with unresolved *K*-lines from the stainless steel components (Fe, Cr, Ni) comprising the stationary source, i.e. the focus electrode and shield surrounding the electrode stack, see Fig. 3.

Operating the tube at 40 kV yields the basic X-ray energy distributions used in mouse imaging. Aluminium filtration can be used to further tailor the spectra. The glass envelope enclosing the X-ray source is Corning 7740 borosilicate glass having a thickness of 1 mm. This corresponds to ~0.7 mm of Al over the energy range studied here so there is some filtering of the beam from the source assembly. Previous studies have demonstrated that a 0.5 mm thickness of aluminium (or silicon dioxide) is sufficient to filter the intense *L*-radiation from the tungsten anode (Boone 2003).

4.5. Half-value layer measurement

From the Results section, half-value-layers of aluminium corresponded to 0.8 mm at 35 kV. 0.9 mm at 40 kV, and 1.0 mm at 45 kV and the effective X-ray energies referenced to these HVLs are 20 keV (0.8 mm), 21 keV (0.9 mm) and 22 keV (1.0 mm), respectively. These energies are in the range of those typical of mouse imaging. The glass envelope enclosing the X-ray source corresponds to ~0.7 mm of Al, and this provide filtration of the X-ray beam as it passes through the glass. Additional filtration may be necessary to optimize the signal to noise ratio and radiation dose efficiency in actual animal experiments.

4.6. Source time to failure

Cold field emission cathodes used in X-ray sources for industrial and medical applications (Brodie and Spindt 1992, Brodie and Schwoebel 1994) were originally based on arrays of etched-wire needle field emitter tips. The most significant impediment to the widespread use of these macroscopic needle sources in X-ray medical imaging applications was that even well below practical pressures obtained in X-ray tubes (~10^{-5} Torr during operation), ion bombardment of the cathode tips resulted in erosion (i.e., sputtering) of the tip and eventual destruction of the cathode. The invention of microfabricated cold cathodes solved this problem by allowing for cathode lifetimes in excess of 10,000 hours (Spindt *et al*. 1983) albeit under operating conditions quite different than those encountered in X-ray tubes, see below. Microfabricated cold cathodes therefore overcame an impediment to the utilization of cold field emission cathodes in medical X-ray tubes, yet in so doing introduced another: greater sensitivity to cathode damage induced by electrical discharge due to their small size and integral gate electrode – as damage can lead to gate-to-base electrical shorts. This has been a major impediment to the incorporation of this technology into practical applications. In a broader sense electrical breakdown induced cathode damage has been a major impediment to the incorporation of field electron emission cathodes into essentially any commercial application with the exception of electron microscopes in which it is straightforward to periodically thermally process the etched-wire cathodes to extend their life.

Present reliability limitations are imposed by damage to the microfabricated cold cathode structure caused by electrical discharges (i.e., voltage breakdown). We have found that the use of intermediate electrodes placed between the cathode and high voltage target electrode help to shield the cathode from participating directly in discharges with the anode target electrode. Nonetheless, when voltage breakdowns occur during operation, there is a tendency for the breakdown to couple into the path of the electron beam and return to the microfabricated cathode.

As mentioned in Section 3.6, both historically and during the course of these experiments the cathode lifetime decreases as the emitted current is increased particularly when high electrostatic fields (and/or voltages) are present on electrodes in the system. Unfortunately one cannot isolate the two because as higher currents are used higher fields are needed to overcome space-charge effects. Typically long lifetimes such as those referred to above have been demonstrated at modest currents and electrode voltages (fields). For example the >10,000 h lifetime was measured under ultrahigh vacuum conditions ($<10^{-9}$ Torr) with a total current of between 2 and 5.5 mA (~ 1 A/cm^2) and cathode to collector (target) voltages of ~ 1kV (field < 1 kV/mm), total current and power levels well below those required for X-ray tube operation. The increased failure rate under high current-high voltage (field) conditions could be due to several possible sources. First there are factors involving cathode fabrication such as inadequate emission uniformity between tips comprising the cathode element and defect densities in films. Processes related to operation include the possibly of the charging of insulating surfaces by electron bombardment. Electron bombardment of insulator surfaces on the cathode can be the result of, for example, primary electrons being reflected from the target, and the bombardment of insulator surfaces elsewhere in the x-ray tube producing secondary electrons that impinge on the cathode insulator. Charging can induce surface breakdown of the insulator. If this occurs on the insulator between the tip and gate electrode of the cathode (see Figure 2), electrical shorting of the electrodes can result. If such events couple into adjacent high voltage electrodes significant power can be dissipated in the cathode structure. Gate-to-tip electrode shorting has been the historical mode by which the cathode is rendered unusable.

Minor damage to the cathode can often be mitigated by using the dielectric shield design pictured in Figure 10b. In this design the dielectric shield placed between the gate electrode and tip electrode helps to prevent electrical shorting, or a contact with low electrical resistance, between these electrodes when there is cathode damage. The result has been a significant improvement in general cathode reliability (Spindt 2010). In the present X-ray tube studies the results discussed in Section 3.6 would also indicate a general decrease in failure rate for the shielded cathodes relative to the standard cathodes.

Table 1 shows some possible key cathode damage mechanisms and how we believe the standard and shielded cathode designs compare. The damage mechanisms certainly have a component due to the presence of high-voltage. Thus, an additional aid to mitigating much of the cathode damage observed may well be to design the high voltage system for operation at ~ 2× the voltages at which it will be routinely operated. Present voltage limitations appear, by visual observation with and image intensifier, to be due to electron emission from the focus electrode and shield enclosing the electrode stack (see Figure 3). We anticipate that appropriate radiuses on the edges and corners on this portion of the assembly would allow for voltage processing to 100 kV.

4.7. Slice Sensitivity Profile

Slice-sensitivity profiles imply expected values and are consistent with the 24° tomographic angle used in this study. With a larger array of X-ray sources spanning a wider tomographic angle, increased resolution in the *z*-axis is clearly possible (Nosrateih *et al*, 2012). While a

high-resolution picture of, for example, tumour perfusion may be limited with the 1.3 mm FWHM slice sensitivity profile, it may still provide the necessary quantitative data for following tumour growth and shrinkage after therapy, especially in the larger rat model.

4.8. Tomographic imaging and flow phantom tomosynthesis

For a thin film transistor based detector, the acquisition time will ultimately be limited by the detector frame rate and not the source array. While the thin film transistor-based detector system used in this study was adequate to demonstrate the potential of multi-source TS, other detector types have faster frame rates. For example, available CMOS detectors (Dexela, Perkin Elmer) have frame rates of up to 70 frames per second with 150 μm pixel dimensions (2 × 2 binning), and can achieve higher resolution (75 μm dimensions to the square detector arrays in 1 × 1 binning mode). Therefore, the potential for higher temporal TS images exists with present-day technology.

In addition to higher temporal resolution using detectors with faster frame rates, the tomographic application for breast or small animal imaging may be performed more optimally with a different geometric arrangement of the X-ray sources. One example would be to use a mounting arrangement where the sources are housed in a curved configuration, the benefits being that the normal ray would be directed towards the detector surface and that an appropriate curved design would compensate for the inverse square law. Of course, a much larger array which spans at least 180° of image data could be used to perform stationary-source computed tomography, however the detector configuration would need to be redesigned and more detectors would be needed.

Vascular flow dynamics in humans have been traditionally captured using digital subtraction angiography (DSA); however, in recent years CT scanners have had the necessary speed of acquisition to provide true three dimensional flow images with high temporal resolution (0.5 sec). The ability to identify vessels in 3D (i.e., individual voxels within a tumour) creates the potential for the assessment of vascular perfusion parameters such as blood volume, vascular perfusion, and time to peak enhancement. Even with the reduced *z*-axis resolution of TS acquisition techniques, we expect similar kinetic flow parameters can be evaluated with accuracy.

5. Conclusions

Microfabricated Spindt type cold cathodes consisting of 50,000 tips in an 0.8 mm^2 area have been used to form X-ray focal spots having minimum dimensions of 0.26 mm × 0.38 mm at 40 kV with 40 mA of beam current. Beam currents of 10 mA at 40 kV were used to demonstrate acquisition of tomographic data sets using digital TS and their reconstruction. Preliminary studies to determine the feasibility of employing the stationary X-ray source based on cold-cathode electron source technology for vascular dynamics studies have also been conducted. Flow through a mouse phantom has been investigated and can be resolved in the tomographic reconstructions at rates up to ~12 ml/min.

X-ray energy spectra from tungsten targets with tube potentials from 35 kV through 50 kV are consistent with standard bremsstrahlung spectra. The X-ray pulse shape from the

stationary source is reasonably consistent between source elements and from one source element as a function of time. Half-value-layer measurements and slice sensitivity profiles yielded values in the anticipated range.

Source reliability, in terms of time to source failure, is not yet at an acceptable level for application of this cathode technology to a commercial stationary X-ray source. Source reliability decreases at high voltage operation as currents were increased above ~10 mA. However, we are presently investigating several possible means to improve the consistency of source lifetime. These involve, for example, better high voltage processing to prevent the occurrence of, even occasional, electrical breakdown events and the use of more resistive silicon cathode substrates to suppress current surges associated with intermittent over-voltage events.

Supplementary Material

Refer to Web version on PubMed Central for supplementary material.

Acknowledgments

The authors gratefully acknowledge many valuable discussions with Christopher Holland and Dr. Capp Spindt of SRI. Phillip Heintz (University of New Mexico Department of Radiology) provided the ionization chamber and assisted with half-value-layer measurements. Microfabricated Spindt tip arrays were made by the vacuum microelectronics group at SRI (Chris Holland, Capp Spindt, Colby Bellew, Kathryn Todd, David Thibert, and Bill Chu).

This research was supported by NIH/NCI grants 1R21CA133433 and 1R21CA131640. Support at University of California Davis from NIH R01 EB002138 is acknowledged. The content is solely the responsibility of the authors and does not necessarily represent the official views of the National Cancer Institute or the National Institutes of Health.

References

Alakhmas M, Bourne R, Rickard M, Ng KH, Pietrzyk M, Brennan PC. Digital tomosynthesis: A new future for breast imaging? Clin. Radiol. 2013; 69:225–236.

Badea CT, Wetzel AW, Mistry N, Pomerantz S, Nave D, Johnson GA. Left ventricle volume measurements in cardiac micro-CT: the impact of radiation dose and contrast agent. Comput. Med. Imaging Graph. 2008; 32:239–250. [PubMed: 18243656]

Badea CT, Johnston SM, Subashi E, Qi Y, Hedlund LW, Johnson GA. Lung perfusion imaging in small animals using 4D micro-CT at heartbeat temporal resolution. Med. Phys. 2010; 37:54–62. [PubMed: 20175466]

Boone JM, Geraghty EM, Seibert JA, Wootton-Gorges SL. Dose reduction in paediatric CT: a rational approach. Radiology. 2003; 228:352–360. [PubMed: 12893897]

Brodie I, Spindt CA. Vacuum Microelectronics. Adv. Electron. Electron Physics. 1992; 83:1–106.

Brodie I, Schwoebel PR. Review: Vacuum microelectronic devices. Proc. IEEE. 1994; 82:1005–1034.

Bushberg, JT.; Seibert, JA.; Leidholdt, EM., Jr; Boone, JM. The Essential Physics of Medical Imaging. Third Edition. New York, New York: Lippincott, Williams, and Wilkins; 2012.

Calderón-Colón X, Geng H, Gao B, An L, Cao G, Zhou Otto. A carbon nanotube field emission cathode with high current density and long-term stability. Nanotechnology. 20:325707. (p. 5). [PubMed: 19620758]

Cronin JL. Modern Dispenser Cathodes. IEE Proc. 1981; 128:19–32.

Ceschia M, Paccagnella A, Sandrin S, Ghidini G, Wyss J, Lavale M, Flament O. Low field leakage current and soft breakdown in ultra-thin gate oxides after heavy ions, electrons or X-ray irradiation. IEEE Trans. Nucl. Sci. 2000; 47:566–573.

Fahrig R, Wen Z, Ganguly A, DeCrescenzo G, Rowlands JA, Stevens GM, Saunders RF, Pelc NJ. Performance of a static-anode/flat-panel X-ray fluoroscopy system in a diagnostic strength magnetic field: A truly hybrid X-ray/MR imaging system. Med. Phys. 2005; 32:1775–1784. [PubMed: 16013735]

Godfrey DJ, McAdams P, Dobbins JT. The effect of averaging adjacent planes for artifact reduction in matrix inversion tomosynthesis. Med. Phys. 2013; 40:021907. [PubMed: 23387755]

Hsieh SS, Heanue JA, Funk T, Hinshaw WS, Wilfley BP, Solomon EG, Pelc NJ. The feasibility of an inverse geometry CDT system with stationary source arrays. Med. Phys. 2013; 40:031904. [PubMed: 23464319]

Jensen KL. Field emitter arrays for plasma and microwave source applications. Plasma Phys. 1999; 6:2241–2253.

Johnson BB, Schwoebel PR, Resnick PJ, Holland CE, Hertz KL, Chichester DL. Field ionization characteristics of an ion source array for neutron generators. J. Appl. Phys. 2013; 117:174906. (p. 9).

Jung HN, Chung MJ, Koo JH, Kim HC, Lee KS. Digital tomosynthesis of the chest: Utility for detection of lung metastasis in patients with colorectal cancer. Clin. Radiol. 2012; 67:232–238. [PubMed: 21939964]

Larsson DH, Lundstrom U, Westermark UK, Henriksson MA, Burvall A, Hertz HM. First application of liquid-metal-jet sources for small animal imaging: High-resolution CT and phase-contrast tumor demarcation. Med. Phys. 2013; 40:021909. (p. 7). [PubMed: 23387757]

Maissel, LI.; Glang, R. Handbook of Thin Film Technology. New York, New York: McGraw-Hill; 1970.

Maltz, JS.; Fuerst, J.; Paidi, A.; Fadler, F.; Bani-Hashemi, AR.; Sprenger, F. Fixed gantry tomosynthesis system for radiation therapy image guidance based on a multiple source x-ray tube with carbon nanotube cathodes; IEEE Symposium on Biomedical Imaging 2009; 2009. p. 1239-1242.

Muller A. Further estimates of the input limits of X-ray generators. Proc. Roy. Soc. A. 1931; 132:646–649.

Niklason LT, Christian BT, Niklason LE, Kopans DB, Castleberry DE, Opsahl-Ong BH, Landberg CE, Slanetz PJ, Giardino AA, Moore R, Albagli D, DeJule MC, Fitzgerald PF, Fobare DF, Giambattista BW, Kwasnick RF, Liu J, Lubowski SJ, Possin GE, Richotte JF, Wei CY, Wirth RF. Digital tomosynthesis in breast imaging. Radiology. 1997; 205:399–406. [PubMed: 9356620]

Nosratieh A, Yang K, Aminololama-Shakeri S, Boone JM. Comprehensive assessment of the slice sensitivity profiles in breast tomosynthesis and breast CT. Med. Phys. 2012; 39:7254–7261. [PubMed: 23231276]

Paulus MJ, Gleason SS, Kennel SJ, Hunsicker PR, Johnson DJ. High resolution X-ray computed tomography: An emerging tool for small animal research. Neoplasia. 2000; 2:62–70. [PubMed: 10933069]

Qian X, Tucker A, Gidcumb E, Shan J, Yang G, Calderon-Colon X, Sultana S, Lu J, Zhou O, Sponk D, Sprenger F, Zhang Y, Kennedy D, Fabrizio T, Jing Z. High resolution stationary digital breast tomosynthesis using distributed carbon nanotube X-ray source array. Med. Phys. 2012; 39:2090. [PubMed: 22482630]

Saito, Y. Carbon nanotube and related field emitters. Weinheim, FRG: Wiley-Vch; 2010.

Schreiber EC, Chang SX. Monte Carlo simulation of a compact microbeam radiotherapy system based on carbon nanotube field emission technology. Med. Phys. 2012; 39:4669–4678. [PubMed: 22894391]

Schwoebel PR, Brodie I. Surface science aspects of vacuum microelectronics. J. Vac. Sci. Technol. B. 1995; 13:1391–1410.

Schwoebel PR, Spindt CA, Holland CE. High current, high current density field emitter array cathodes. J. Vac. Sci Technol. B. 2005; 23:691–693.

Schwoebel PR. Field emission arrays for medical imaging. Appl. Phys. Lett. 2006; 88:113902-1–113903-3.

Sechopoulos I. A review of breast tomosynthesis. Part. I. The image acquisition process. Med. Phys. 2013; 40:014301. [PubMed: 23298126]

Shan J, Chtcheprov P, Tucker AW, Lee YZ, Wang X, Foos D, Heath MD, Lu J, Zhou O. Stationary chest tomosynthesis using a CNT x-ray source array. Proc. SPIE. 2013; 8668:86680E.

Smith, DJ.; Bui, A-P.; Michael, JD.; Aceto, SC.; Marquard, K.; Brewer, JE. Stable, high current density carbon nanotube field emission devices; Vacuum Nanoelectronics Conference, 2013 26th International; 2013. p. 1-2.

Spindt, Charles A.; Holland, Christopher E.; Stowell, Robert D. Field emission cathode array development for high-current-density applications. Appl. Surf. Sci. 1983; 16:268–276.

Spindt, C.; Holland, CE.; Schwoebel, PR. A reliable improved Spindt cathode design for high currents. IEEE Vacuum Electronics Conference (IVEC); IEEE International; 2010. p. 201-202.

Sprenger F, Calderon X, Gidcumbb E, Lu J, Qian X, Spronk D, Tuckerb A, Yang G, Zhou O. Stationary digital breast tomosynthesis with distributed field emission X-ray tube. Proc. SPIE. 2011; 7961:878280. [PubMed: 21617760]

Toshiba 2014 See for example specifications for Toshiba Cine-Fluorographic tube E7902X.

Tucker AW, Lu J, Zhou O. Dependency of image quality on system configuration parameters in a stationary digital breast tomosynthesis system. Med. Phys. 2013; 40:031917. [PubMed: 23464332]

Uribe, J., et al. Multisource Inverse-Geometry CT-Prototype System Integration; Nuclear Science Symposium Conference Record (NSS/MIC) 2010 IEEE; 2010. p. 2678-2581.

Whaley DR, Gannon BM, Heinen VO, Kreischer KE, Holland CE, Spindt CA. Experimental demonstration of an emission-gated travelling-wave tube amplifier. IEEE Trans. Plasma Science. 2002; 30:998–1008.

Whaley DR, Duggal R, Armstrong CM, Bellew CL, Holland CE, Spindt CA. 100 W operation of a cold cathode TWT. IEEE Trans. Electron Devices. 2009; 56:896–905.

Xu NS, Huq SE. Novel cold cathode materials and applications. Materials Science and Engineering R. 2005; 48:47–189.

Xu X, Kim J, Laganis P, Schulze D, Liang Y, Zhang T. A tetrahedron beam computed tomography benchtop system with a multiple pixel field emission x-ray tube. Med. Phys. 2011; 38:5500. [PubMed: 21992368]

Yang K, Kwan ALC, Miller DF, Boone JM. A general geometric calibration method for cone beam CT systems. Med. Phys. 2006; 33:1695–1706. [PubMed: 16872077]

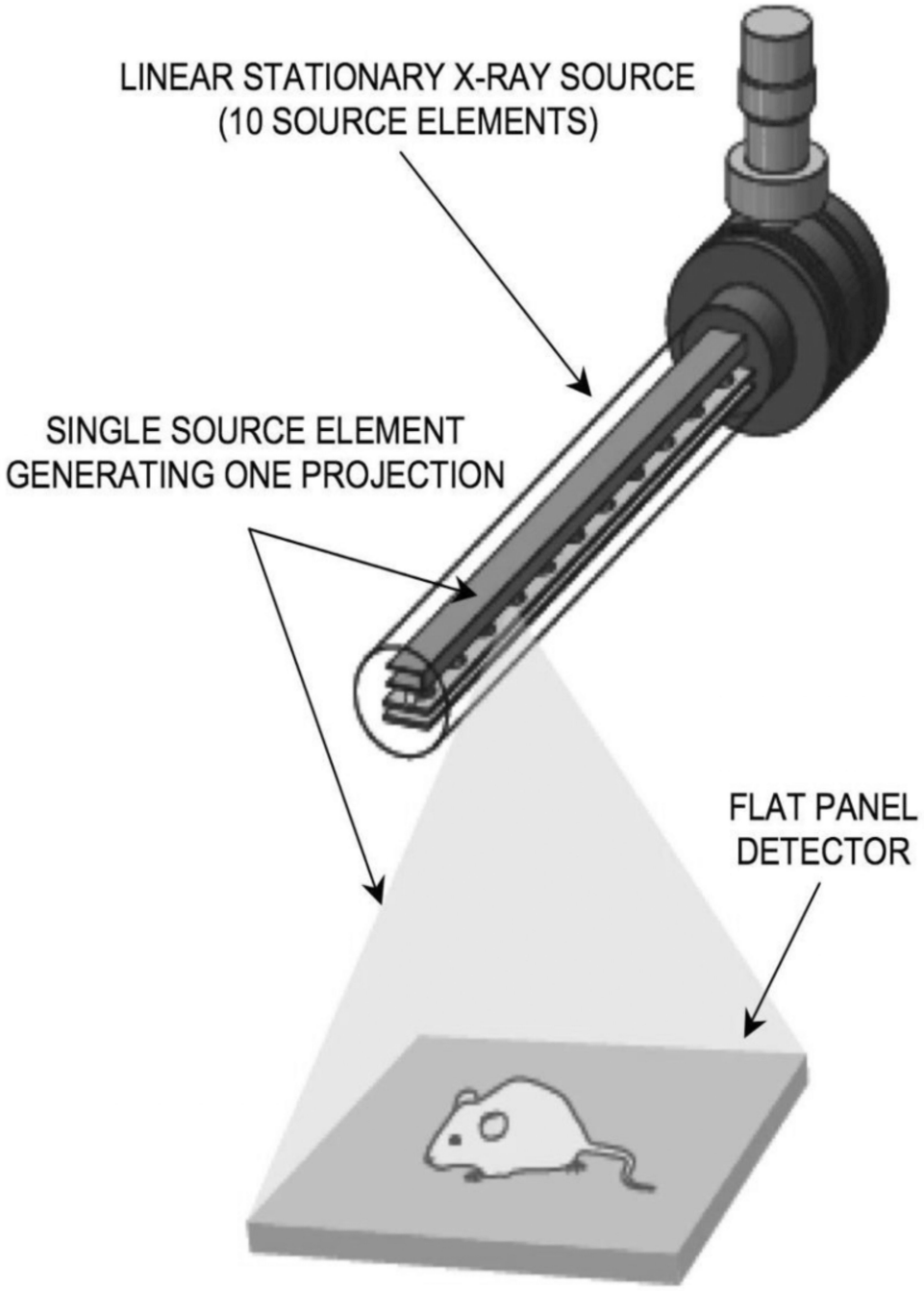

Figure 1.
A schematic of a stationary X-ray source-stationary detector system used for small animal vascular dynamics studies.

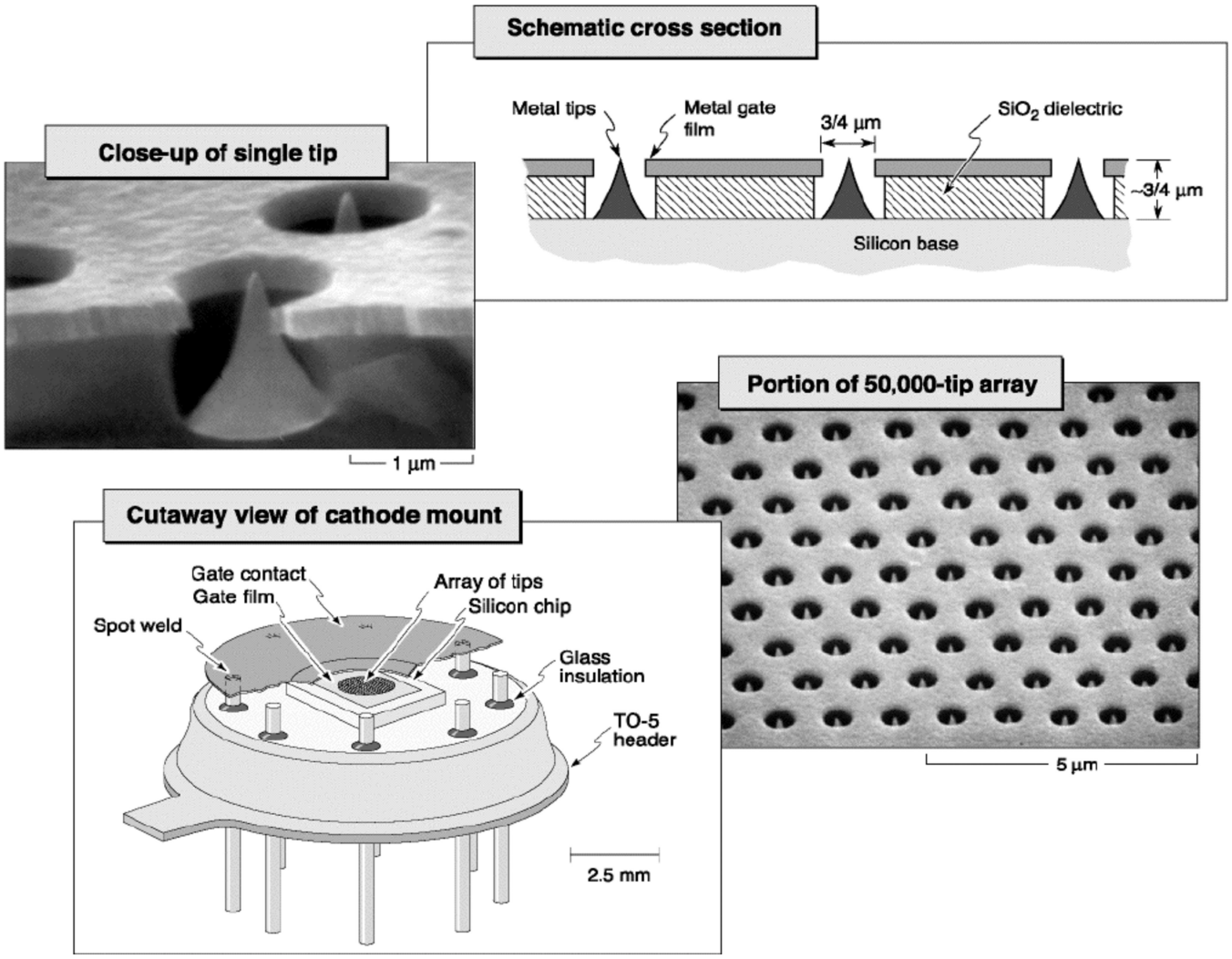

Figure 2.

Schematic and electron micrographs of a typical Spindt-type cathode and the TO-5 header mount.

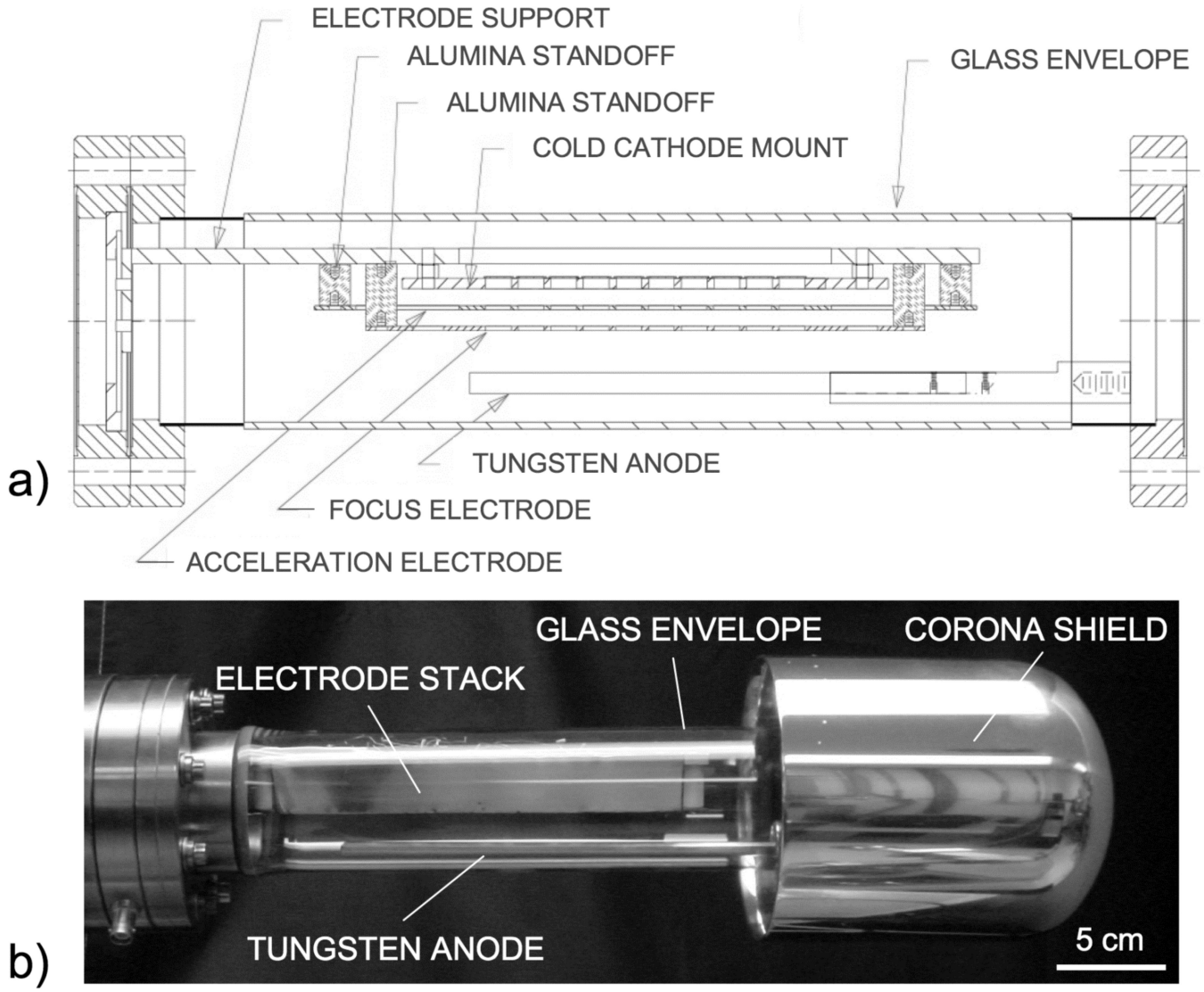

Figure 3.
Schematic and photograph of the 10-element linear stationary X-ray source.

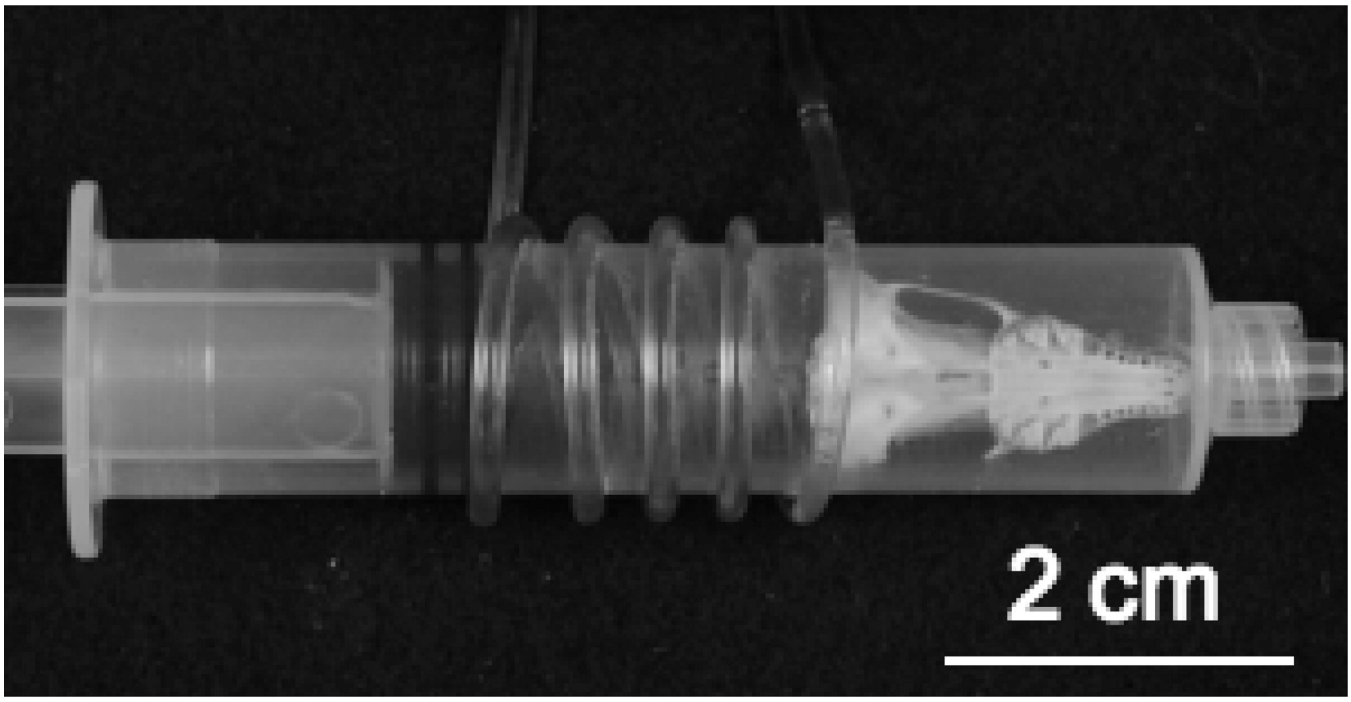

Figure 4.
Photograph of the mouse flow phantom.

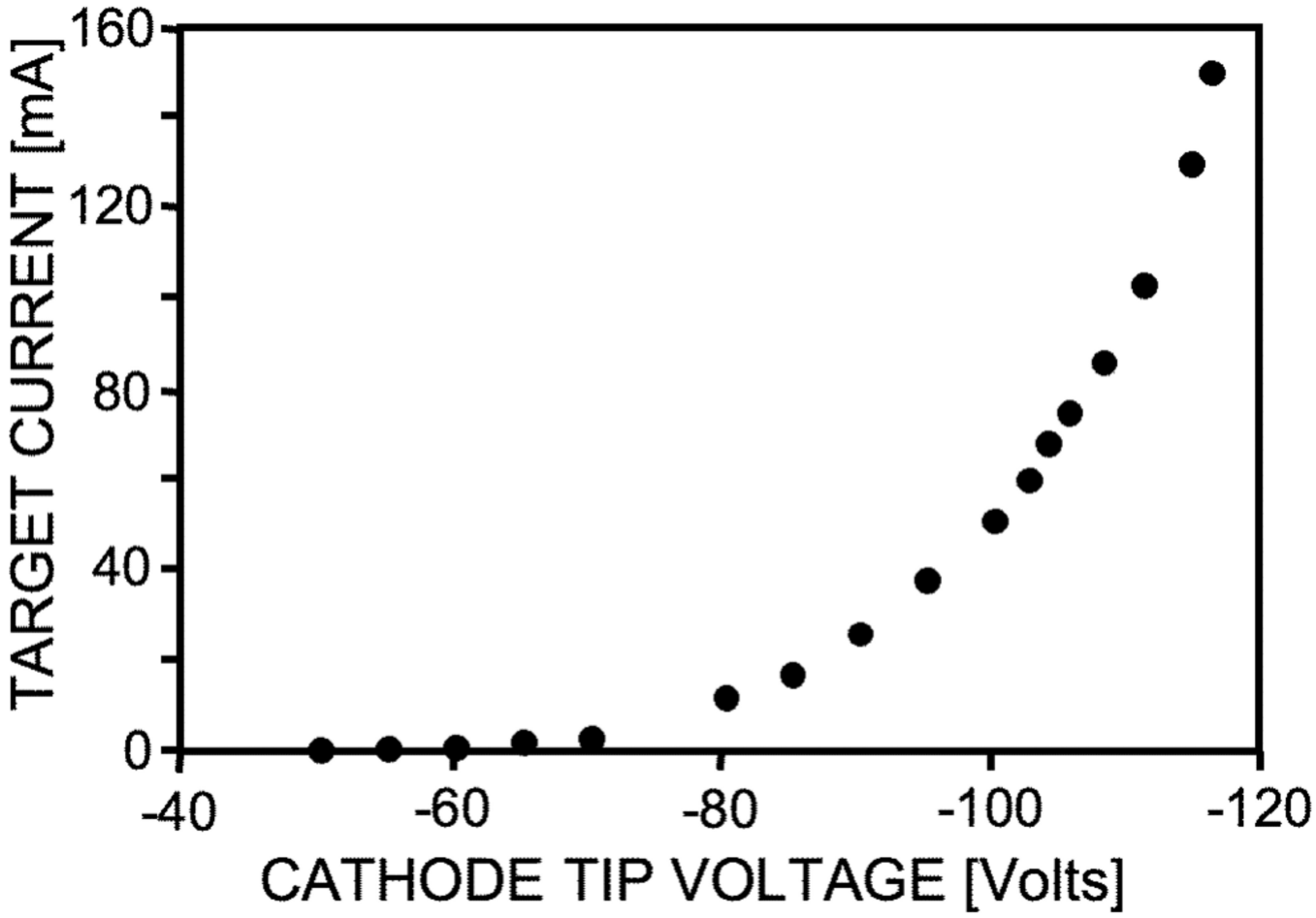

Figure 5.
Current-voltage characteristics of a Spindt type cathode (Target voltage = 10 kV; Current pulse width = 1 ms; 50,000-tip array in an area of 0.8 mm^2).

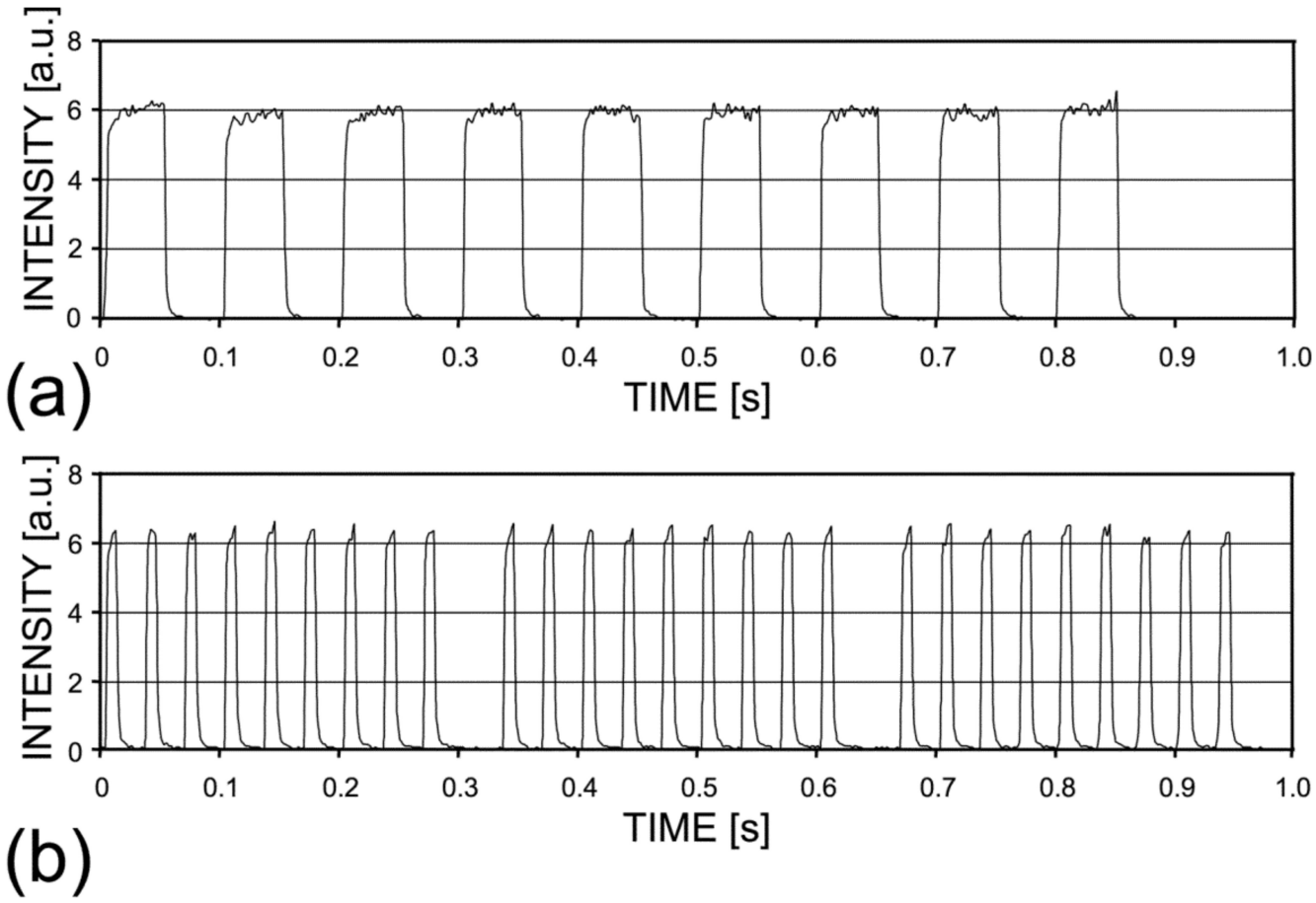

Figure 6.

X-ray pulse shape versus time plots for 10 mA of electron current at 40 kV. (a) 10 Hz and (b) 30 Hz.

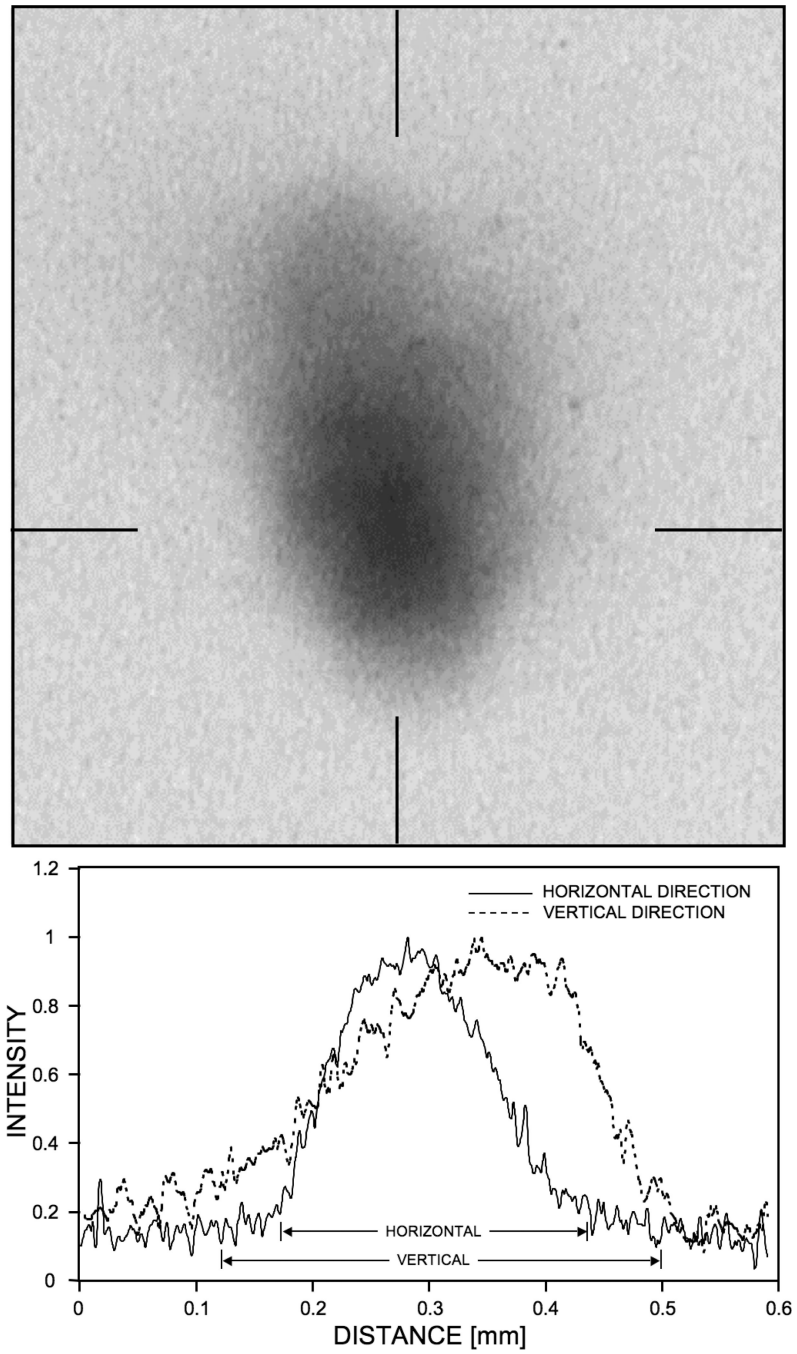

Figure 7.

Pinhole camera image and corresponding intensity contours of the X-ray focal spot formed at 40 kV and 40 mA.

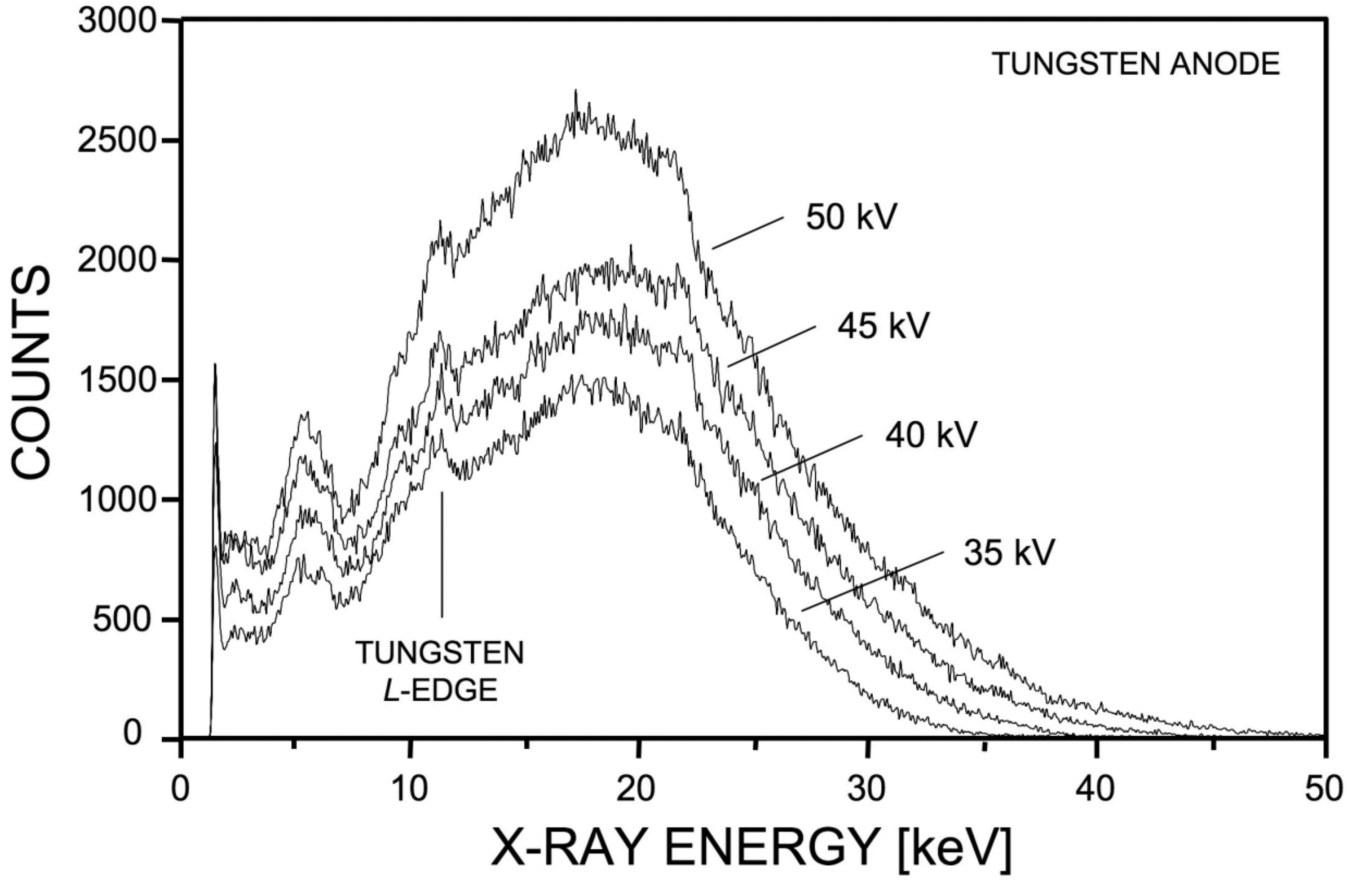

Figure 8.
X-ray spectrum from a tungsten anode at voltages of 35, 40, 45, and 50 kV.

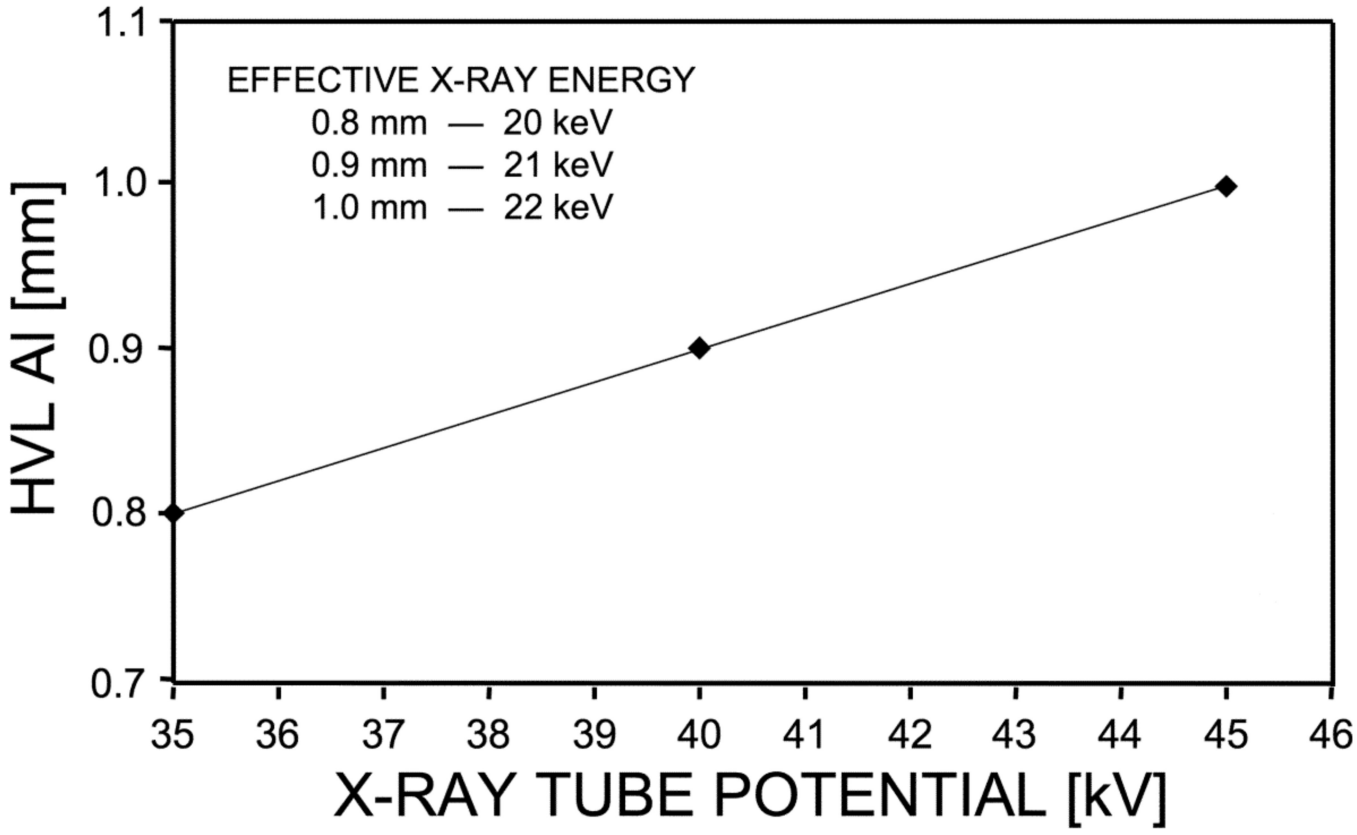

Figure 9.
X-ray tube potential versus half-value-layer of aluminium.

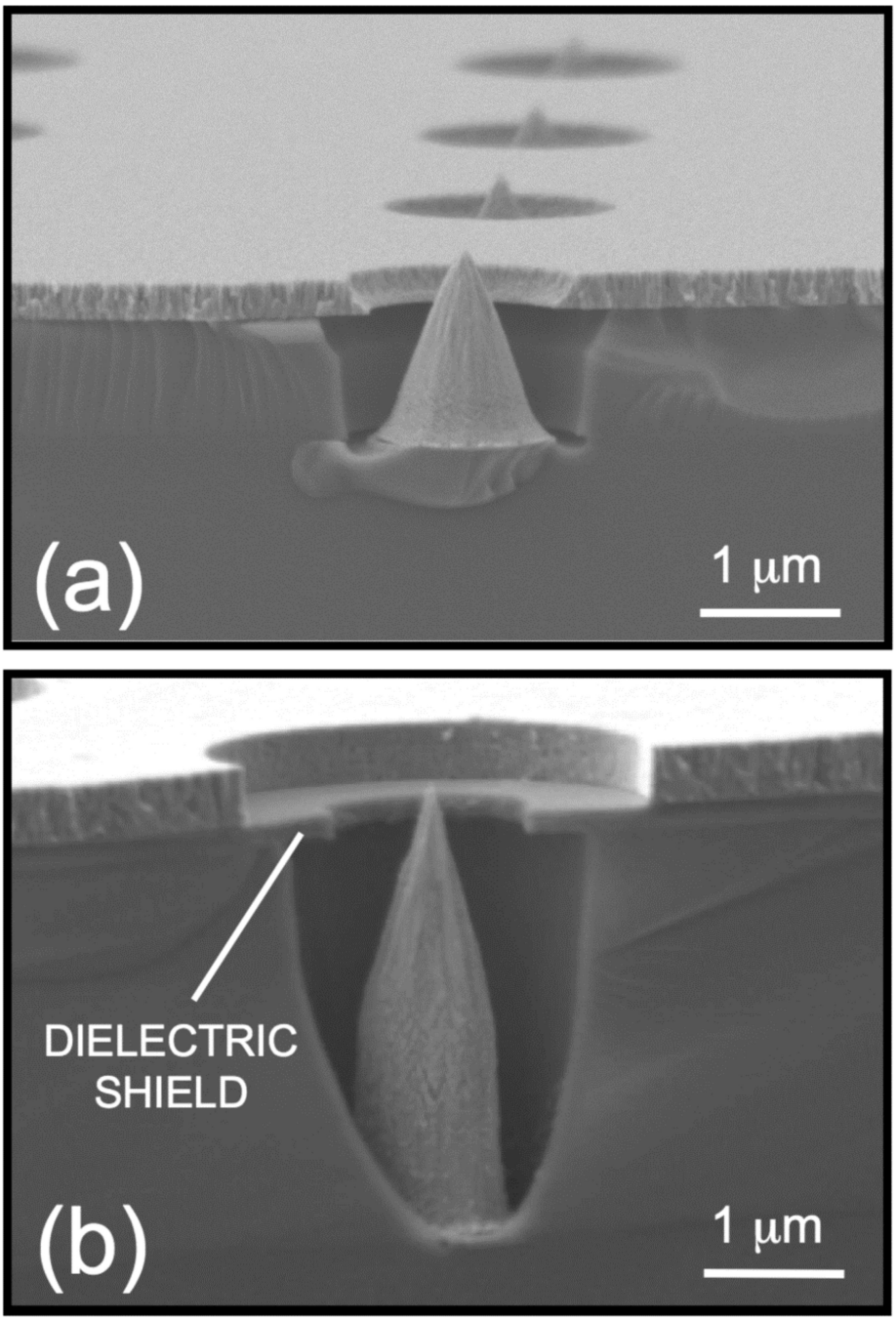

Figure 10.
Photographs of (a) the Spindt cold-cathode depicted in its standard form and (b) one incorporating a dielectric shield.

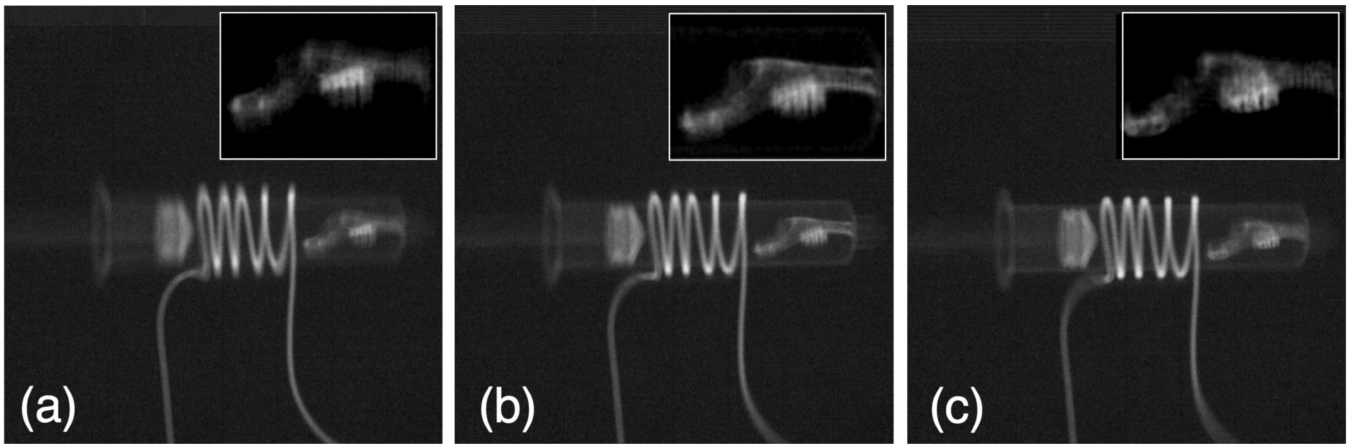

Figure 11.

Three tomographic images showing that different tomographic planes are visible. The inserts show enlarged images of the skull, see text. The entire reconstructed data set can be viewed in the supplementary data file associated with the online paper.

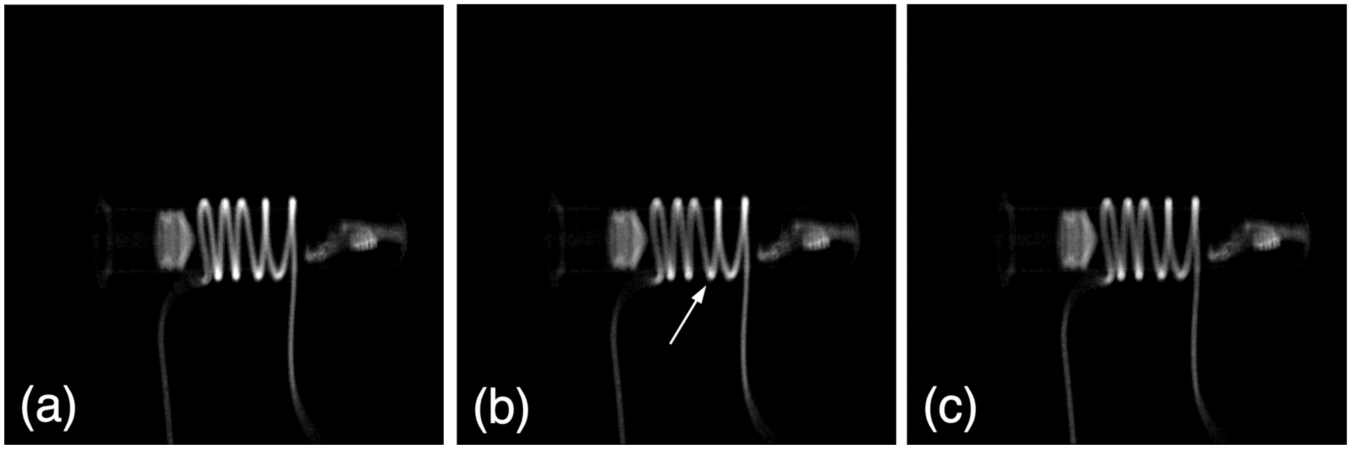

Figure 12.

A series of images of one projection from each tomographic data set during washout. (a) The tubing surrounding the syringe body is completely filled with contrast agent (t = 0.33 s), (b) The contrast agent is being flushed out from left-to right. To the left of the location denoted by the arrow the tubing is full of water (t = 0.67 s), and (c) The tubing surrounding the syringe body is completely filled with water (t = 1.33 s).

Table 1

Cathode damage mechanisms.

Mechanism	Standard Cathode	Shielded Cathode
X-ray System Precipitated		
1. High voltage breakdown		
A) Involving cathode as an electrode	P	P
B) Not involving cathode as an electrode		
- Couple voltage pulse into cathode causing excessive emission	P	P
- Evaporate material onto cathode tips	P	P
- Evaporate material onto cathode insulating surfaces	P	U
2. Tip-gate insulator (Thermal SiO_2) breakdown		
A) Surface breakdown: Not triple point induced[a, b]	P	U
3. Ion bombardment induced tip erosion[c]	U	U
4. Radiation damage of cathode insulators[d]	U	U
Cathode Precipitated		
1. Tip-gate insulator (Thermal SiO_2) breakdown		
A) Surface breakdown: Triple point induced[e]	U	U
B) Bulk breakdown[f]	U	U
2. Cathode tip failure		
A) Field stress induced mechanical failure[g]	U	U
B) Other modes (*e.g.* fabrication defects, contaminant desorption)	P	P

P = Possible U = Unlikely

[a] Surface breakdown caused by insulator charging due to electron bombardment. Electrons originating from primaries reflected from target, etc.

[b] The shielded cathode design tends to protect the insulator surface of the cathode from direct bombardment

[c] Not an issue at our operating pressures of 10^{-10} Torr even for operational times of many 1000's of hours (Brodie and Spindt 1992)

[d] X-ray doses are too low at this point to cause a significant to the breakdown fields of the SiO_2 insulator (Ceschia *et al.* 2000)

[e] Unpublished modelling results have shown that electric fields at the tip electrode-insulator-vacuum junction are very low.

[f] Applied fields are well below those for bulk breakdown of the thermal SiO_2 insulator

[g] The cathode tips have been shown to regularly support nearly 100× the field stress associated with electron emission fields (Johnson *et al.* 2013)